J Braz. Soc. Mech. Sci. Eng. (2015) 37:1569–1589
DOI 10.1007/s40430-015-0369-6

TECHNICAL PAPER

Development of a time domain boundary element method for numerical analysis of floating bodies' responses in waves

Rafael A. Watai[1] · **Felipe Ruggeri**[1] · **Claudio M. P. Sampaio**[1] · **Alexandre N. Simos**[1]

Received: 23 June 2014 / Accepted: 4 May 2015 / Published online: 15 May 2015

Abstract This article presents the development of a numerical tool for seakeeping simulations of marine systems using a time domain boundary element method based on Rankine sources. The formulation considers two initial boundary value problems defined for the velocity and acceleration potentials, the last being used to avoid numerical problems in calculating the time derivatives of the velocity potential. A fourth-order Runge–Kutta method is used for the time marching of the problem, which consists in the integration of the free surface conditions and body equations of motion. Numerical test cases are presented for bodies with simplified geometries, such as an hemisphere and a circular section cylinder. Exciting forces, added mass and radiation damping coefficients, and motions response amplitude operators are compared to analytical and numerical data, presenting a very good agreement. Furthermore, the numerical method is applied to a floating production storage and Off-loading unit and the results are verified with experimental data carried out in the hydrodynamic calibrator of the University of Sao Paulo. By means of these investigations, we have verified that the developments performed so far are correct and new extensions, therefore, may be planned for more complex applications.

Keywords Boundary element method · Time domain simulations · Rankine sources · Seakeeping analysis

1 Introduction

The exploration of oil and gas fields in ultradeep water, such as the Brazilian pre-salt layer, demands a considerable amount of investments to be concretized. The necessity of long production risers, sophisticated pump and valve systems, and the conduction of maintenance services results in high operational costs, requiring significant oil production to make the process feasible. In this context, seakeeping analysis is a topic of great importance for the design of floating oil production units, since their response in waves will define whether the structure will operate properly or not. In fact, better designs should help reduce the production downtime, especially under harsh environmental conditions, which consequently improves the production efficiency and reduce costs.

In current practice in the area of ocean engineering, experimental activities with scaled models have provided great knowledge and understanding of complex phenomena involving the interaction between floating structures and environmental conditions, such as waves, wind and current. The constraints involved in scaled model tests are related to the difficulties in relation to physical limitations of the basins, especially in modeling systems that operate in deep waters. Moreover, since the tests require high costs and considerable time to be performed, presently they have been more used for final verification and not as a prediction tool for earlier stages of the design.

The use of a numerical approach has become increasingly popular in the various stages of engineering designs, mainly due to the growth of computational power and development of new techniques for numerical processing. In this context, the use of numerical methods that deal with potential flow boundary value problems, such as the boundary element method (BEM), is widely applied throughout

---

Technical editor: Celso Kazuyuki Morooka.

✉ Rafael A. Watai
rafael.watai@usp.br

[1] Numerical Offshore Tank, Av. Prof. Mello Moraes 2231, Cidade Universitaria, Sao Paulo, Brazil

the design stages for solving hydrodynamic issues. The use of numerical methods reduce the demand of experimental tests between the stages of conception and final verification; however, it does not eliminate their necessity, which usually provides essential contributions on the validation and extension of numerical methods.

A mixed approach based on numerical methods combined with experimental data then emerges as an interesting approach for handling the problem. This idea is being followed by the Numerical Offshore Tank of the University of Sao Paulo (TPN-USP) since 2000, which has as one of the main goals the development of a simulator that can handle a fully coupled solution of body hydrodynamics, mooring lines and environmental conditions. Moreover, the laboratory also counts on with a hydrodynamic calibrator wave basin (CH-TPN), which is used for the calibration of the simulator.

Specifically concerning the wave problem, the TPN simulator uses the BEM code implemented in WAMIT software [1] to calculate linear potential hydrodynamic coefficients in the frequency domain which are properly transposed to the time domain following the equations derived by [2]. However, one should realize that some inconsistencies may appear if the body acquires large amplitudes of motions around its mean initial position, disobeying the original linear assumption established for the hydrodynamic load calculations. Another problem is the body seakeeping evaluation in scenarios of ultradeep water, in which the dynamics of the risers and mooring lines may play a role in the oil platform motions, but is disregarded in the hydrodynamic calculations. Furthermore, this procedure limits the study of the fully nonlinear problem, since in the frequency domain only weakly nonlinear problems may be handled.

The calculation of the hydrodynamic problem in the time domain then arises as an interesting alternative to overcome these problems, since it may be coupled to the body equations of motion, solved by the dynamic simulator. In comparison to models mathematically treated in the frequency domain, this approach allows us a straightforward addressing for future extensions of nonlinear descriptions of both the hydrodynamic and the dynamic problems. Such extensions would enable us, for example, to consider the instantaneous body wetted surfaces to account for the body motions induced by risers and mooring lines and also to deal, in a more satisfactory way, with the viscous damping effects that as a nonlinear phenomena is commonly modeled by a quadratic term involving the body velocity.

Numerical solutions of the transient wave–body interactions using BEM is normally segregated into two different categories based on the type of singularity employed in the method implementation. The first type uses the transient Green's function as the elementary singularity, which satisfies Laplace's equation and all the boundary conditions except the body boundary ones; see for instance [3]. The major advantages of such a scheme are the satisfaction of the radiation and linear free surface conditions and, therefore, only the wet body surface must be discretized.

The second type, introduced by [4, 5], applies the simple Rankine source as the elementary singularity, which is mainly motivated by the resulting flexibility in the choice of free surface conditions to be satisfied, being the sole alternative for the calculation of nonlinear flows and a more suitable choice for problems involving bodies with forward speed, as discussed by [6, 7]. Moreover, different bottom geometries than the flat shape may be analyzed by distributing the sources over its surface, as recently applied by [8].

Despite the fact that Rankine sources do not satisfy any boundary condition automatically, its application is simpler than using the transient Green's function. In fact, Green's function demands the use of accurate algorithms to be evaluated and results in extensive CPU and memory requirements for the convolution integral computations. In addition, it does not permit the method extension for the calculation of nonlinear wave problems, which is a medium-term goal of our research.

For these reasons, a time domain BEM based on the exclusive use of Rankine sources (Rankine panel method) is developed in the present paper. In this version of the numerical method, the nonlinear effects originated from the presence of the unknown free surface and body surface positions are neglected, whereas the three dimensionality feature of the fluid flow problem is retained. Independently of its own practical interest, which has given favorable results to many problems regarding floating body dynamics, the robust and accurate solution of this linear problem is a very useful first stage before handling the complete nonlinear problem.

In this sense, the work of [9] was followed and a low-order panel method is applied here, in which the mean surfaces are discretized by plane quadrilateral panels that remain fixed during all the simulation. Time domain simulations require an accurate prediction of the pressure field to guarantee a consistent and stable numerical algorithm. A main concern is the properly evaluation of the velocity potential time derivative that depending on the numerical scheme applied may give rise to numerical instabilities. Bearing this in mind, following references [10, 11], the problem is formulated by means of two initial boundary value problems defined for the velocity and acceleration potentials, the latter being used to avoid numerical problems in calculating the time derivatives of the velocity potential and consequently the pressure field.

The time marching of the problem is performed by a fourth-order Runge–Kutta method (RK4), which provides high accuracy and stability to the algorithm. Furthermore, a numerical damping zone is applied to account for wave absorption in part of the free surface, avoiding spoiling the solution by the waves reflected from the domain boundaries.

The implemented numerical tool is firstly tested by solving the diffraction and radiation problems with bodies of simplified geometries, such as the hemisphere and the circular cylinder. One step forward, free floating simulations with the same body geometries are presented. In these calculations, different meshes varying the numbers of body and free surface panels are investigated. The results are compared to the analytical data presented in [24] and to numerical values obtained with the well-validated software WAMIT.

More complex evaluations are carried out with a floating production storage and off-loading (FPSO) unit hull by performing free floating simulations. Based on the linear regime, the response amplitude operators (RAO) motions of the unit are compared to experimental data obtained in campaigns carried out in the CH-TPN. Moreover, direct comparisons of the motion time series induced by a regular wave is also presented. In general, all the results show favorable agreements with the experimental data.

The theoretical formulation of the problem is presented in Sect. 2, followed by the description of the numerical method, which is discussed in Sect. 3. Numerical test case results concerning the solution of the so-called diffraction and radiation problems are presented in Sect. 4, which also includes the free floating motion calculations for bodies with simplified geometries. In Sect. 5, a brief description of the experimental campaign carried out with an FPSO small-scale model is presented, from which data is used for the verification of our numerical method. Finally, the conclusions of this research are presented in Sect. 6.

2 Theoretical formulation

The problem of a floating body interacting with free surface gravity waves is considered here. In this situation, incoming waves that propagate on a free surface are disturbed by the floating bodies inducing unsteady forces and moments due to the generation of pressure changes in the fluid. Floating bodies then respond acquiring translational and rotational motions, which also force the fluid to move. Mathematical description of this problem may result in different governing equations depending on the assumptions on the motions of the body and the fluid concerning its free surface. Moreover, it is usual to separate the equations that describe the behavior of the fluid and the floating body, which are then linked again by appropriate equations and matching conditions that define the wave–body formulations.

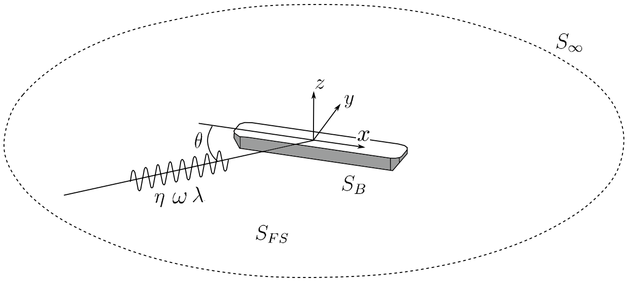

Fig. 1 Definition of the coordinate systems

Let us define three mutually perpendicular unit vectors $\mathbf{e}_1$, $\mathbf{e}_2$, and $\mathbf{e}_3$ that form the basis of the Cartesian coordinate system, in which the hydrodynamic problem and the body motions are described. Figure 1 illustrates a body floating somewhere in the sea in which incoming gravity waves propagate on a free surface S_{FS} with angular frequency ω, length λ and in a direction which makes an angle θ with the x-axis of the established reference frame.

Focusing our analysis in the fluid, we consider an arbitrary control volume Ω delimited by a surface $\partial\Omega$ with normal vector $\mathbf{n} = (n_x, n_y, n_z)$ pointing outward the domain. The fluid flow velocity field is then defined by $\mathbf{v} = (u, v, w)$, in which $u(x, y, z, t)$, $v(x, y, z, t)$ and $w(x, y, z, t)$ are the scalar components of the velocity field at time t, at a point with spatial coordinates (x, y, z).

We consider the flow to be irrotational and incompressible, whereas the fluid is assumed to be inviscid and homogeneous, allowing the velocity field to be defined by the gradient of the potential scalar field or velocity potential Φ:

$$\mathbf{v} = \nabla\Phi. \tag{1}$$

In this sense, the equation of mass conservation is stated by Laplace's equation (2), whereas the conservation of linear momentum is expressed by Bernoulli's equation (3).

$$\nabla^2\Phi = 0 \tag{2}$$

$$\frac{\partial\Phi}{\partial t} + \frac{1}{2}(\nabla\Phi \cdot \nabla\Phi) + gz = -\frac{p - p_0}{\rho} + C(t), \tag{3}$$

where p_0 is the atmospheric pressure and $C(t)$ is a constant dependent on time, normally omitted since it can be absorbed into the velocity potential by redefining the latter without loss of generality of the solution.

Since there are an infinite number of solutions to Laplace's equation, unique solutions for Φ are calculated particularizing the solutions by the imposition of boundary conditions which, in simple words, are necessary to match the dynamics and kinematic of the fluid with the physical boundaries of the fluid domain Ω, such as the wet surface of the floating body $S_{\mathrm{B}}(t)$, the sea bottom surface S_{BO} and the free surface $S_{\mathrm{FS}}(t)$.

The free surface $S_{\mathrm{FS}}(t)$ demands the description of a kinematic and a dynamic boundary condition. Although the air phase could also be modeled as incompressible, since the Mach number is negligible for the application studied, the present work only evaluates the water phase. In the context of nonbreaking waves, the free surface boundary should be understood as a surface that always segregates the air phase from the water phase, acting as a membrane that avoids the "mixture" between both. The ideal fluid hypothesis is used and, hence, the fluid particles may have only tangential velocities concerning the free surface, but not normal ones.

Kinematic condition (4) states that the velocity of the fluid and the free surface boundary must be equal. The free surface adjacent particles remain in the free surface, with the elevation being described as a function η. The condition obtained is nonlinear, since it is the product of the potential and free surface elevation partial derivatives, and is applied at the actual free surface position, which is unknown a priori, leading to a difficult condition to be satisfied generally.

$$\frac{\mathrm{D}}{\mathrm{D}t}(z-\eta)=\frac{\partial\Phi}{\partial z}-\frac{\partial\eta}{\partial t}-\frac{\partial\Phi}{\partial x}\frac{\partial\eta}{\partial x}-\frac{\partial\Phi}{\partial y}\frac{\partial\eta}{\partial y}=0 \quad \text{on } z=\eta(x,y,t). \tag{4}$$

In addition, dynamic condition imposes that, neglecting the surface tensions, the pressure on the free surface must be equal to the atmospheric pressure, enforcing the balance of forces in the free surface membrane. The flow pressure is described by Bernoulli's equation and the atmospheric pressure can be defined as zero, leading to Eq. (5). It should be noticed that this condition is also nonlinear due to the quadratic velocity term and by the fact that it is applied in an unknown position:

$$\frac{\partial\Phi}{\partial t}+\frac{1}{2}(\nabla\Phi\cdot\nabla\Phi)+gz=0 \quad \text{on } z=\eta(x,y,t). \tag{5}$$

The boundary conditions associated with the floating body wet surface $S_{\mathrm{B}}(t)$ and sea bottom surface S_{BO} are mathematically described by Neumann conditions which impose that the fluid particles may not penetrate these surfaces. For the sea bottom and other time-independent surfaces that may be present in the problem, this is represented by the well-known zero-flux condition (6):

$$\nabla\Phi\cdot\mathbf{n}=\frac{\partial\Phi}{\partial n}=0 \quad \text{on } S_{\mathrm{BO}}. \tag{6}$$

The conditions on the submerged surfaces of floating bodies and other time-dependent surfaces are treated in a very similar way as the bottom surface. Nevertheless, the motion of these boundaries influences the motion of the fluid at their surroundings, requiring compatibility of the fluid and surface velocities to guarantee an impermeability condition, as presented in Eq. (7):

$$\nabla\Phi\cdot\mathbf{n}(t)=\frac{\partial\Phi}{\partial n}=\frac{\partial\boldsymbol{\delta}}{\partial t}\cdot\mathbf{n}(t) \quad \text{on } S_{\mathrm{B}}(t), \tag{7}$$

where $\boldsymbol{\delta}$ is the time-dependent displacement of the floating body defined in terms of the translational $\boldsymbol{\xi}_{\mathrm{T}}(t)=(\xi_1,\xi_2,\xi_3)$ and rotational $\boldsymbol{\xi}_{\mathrm{R}}(t)=(\xi_4,\xi_5,\xi_6)$ displacements, and of $\mathbf{r}$ that is the position vector of a point on the body surface relative to the body center of gravity:

$$\boldsymbol{\delta}(t)=\boldsymbol{\xi}_{\mathrm{T}}(t)+\boldsymbol{\xi}_{\mathrm{R}}(t)\times\mathbf{r}. \tag{8}$$

Body motions, in turn, are defined by solving Newton's second law equation, assuming the body mass as constant, small angles and that the only external loads are the gravity and flow pressure:

$$\mathbf{M}\frac{\partial^2\boldsymbol{\xi}}{\partial t^2}=\begin{pmatrix}\mathbf{F}\\ \mathbf{M}_O\end{pmatrix}, \tag{9}$$

where $\boldsymbol{\xi}=(\xi_1,\xi_2,\xi_3,\xi_4,\xi_5,\xi_6)$ and $\mathbf{M}$ are the matrix containing the body mass and moments of inertia. Moreover, $\mathbf{F}$ and $\mathbf{M}_O$ are vectors containing the external forces and moments in relation to a pole O, respectively.

The last, but not less important than the other boundary conditions is the radiation condition, which apart from making the problem unique also enforces that the waves generated by the bodies are outgoing waves only and do not reflect somewhere allowing these waves to interfere with the body motions again.

To conclude this initial boundary value problem (IBVP), an initial condition must be imposed at the free surface so as to determine the subsequent fluid motions. As demonstrated by [3], for flows beginning from the rest, we may set the velocity potential at the initial instant $t=0$ s to:

$$\Phi=0 \quad \text{on} \quad t=0\,s. \tag{10}$$

Although Laplace's equation is linear homogeneous differential, the boundary conditions present several sources of nonlinearities and in some cases must be applied in time-dependent surfaces not known in advance, which makes the problem very complex for solving. Despite this complexity, numerical algorithms that deal with this fully nonlinear problem are becoming popular in recent years, mainly because of huge increase in computer processing capacity. However, most of them are still limited to bi-dimensional studies or very simple three-dimensional geometries and consequently restrict the possibilities of simulating the behavior of real ship vessels, oil platforms or the hydrodynamic interactions involved in multi-body arrangements. Therefore, in this first stage of the research, we decided to linearize the formulation and develop a linear computational code in which the mathematical derivations are presented in the next items.

2.1 Linear formulation

To linearize the problem, we use the well-known perturbation technique using expansions in Stokes series, as also applied by [3], in terms of a small parameter $\varepsilon \ll 1$. With this approach, we may identify and collect terms of order up to ε for a linear problem and consequently higher orders for the other problems. The method proposes the problem to be solved by splitting the original problem into a collection of linear problems (one for each order), solving them successively by imposing the solutions of the lower-order problem into the higher-order ones. Thus, to obtain a linear formulation, we perturb all the variables involved using the small parameter ε and substitute them in the set of nonlinear equations already presented. The velocity potential of order zero vanishes because the problem has no forward speed, and the position and normal vectors of order zero represent their mean values, i.e., the vectors when the bodies are at rest. The expansions of the velocity potential Φ, wave elevation η, normal vector $\mathbf{n}$ and translational $\boldsymbol{\xi}_{\mathrm{T}}$ and rotational $\boldsymbol{\xi}_{\mathrm{R}}$ body motions are presented in (11), (12), (13), (14) and (15), respectively. Hereafter, the horizontal bar $(\bar{\ })$ over the variables means the zero-order values and the superscript ${}^{(i)}$ means the variable order.

$$\Phi = \bar{\Phi} + \varepsilon\Phi^{(1)} + \varepsilon^2\Phi^{(2)} + \mathcal{O}\left(\varepsilon^3\right), \tag{11}$$

$$\eta = \bar{\eta} + \varepsilon\eta^{(1)} + \varepsilon^2\eta^{(2)} + +\mathcal{O}\left(\varepsilon^3\right), \tag{12}$$

$$\mathbf{n} = \bar{\mathbf{n}} + \varepsilon\mathbf{n}^{(1)} + \varepsilon^2\mathbf{n}^{(2)} + \mathcal{O}\left(\varepsilon^3\right), \tag{13}$$

$$\boldsymbol{\xi}_{\mathrm{T}} = \bar{\boldsymbol{\xi}}_{\mathrm{T}} + \varepsilon\boldsymbol{\xi}_{\mathrm{T}}^{(1)} + \varepsilon^2\boldsymbol{\xi}_{\mathrm{T}}^{(2)} + \mathcal{O}\left(\varepsilon^3\right), \tag{14}$$

$$\boldsymbol{\xi}_{\mathrm{R}} = \bar{\boldsymbol{\xi}}_{\mathrm{R}} + \varepsilon\boldsymbol{\xi}_{\mathrm{R}}^{(1)} + \varepsilon^2\boldsymbol{\xi}_{\mathrm{R}}^{(2)} + \mathcal{O}\left(\varepsilon^3\right). \tag{15}$$

Progressing, the velocity vector can be written by derivation of (14) and (15) in time providing (16) and (17):

$$\frac{\partial\boldsymbol{\xi}_{\mathrm{T}}}{\partial t} = \varepsilon\frac{\partial\boldsymbol{\xi}_{\mathrm{T}}^{(1)}}{\partial t} + \varepsilon^2\frac{\partial\boldsymbol{\xi}_{\mathrm{T}}^{(2)}}{\partial t} + \mathcal{O}\left(\varepsilon^3\right), \tag{16}$$

$$\frac{\partial\boldsymbol{\xi}_{\mathrm{R}}}{\partial t} = \varepsilon\frac{\partial\boldsymbol{\xi}_{\mathrm{R}}^{(1)}}{\partial t} + \varepsilon^2\frac{\partial\boldsymbol{\xi}_{\mathrm{R}}^{(2)}}{\partial t} + \mathcal{O}\left(\varepsilon^3\right). \tag{17}$$

The next step would be the substitution of the perturbed quantities into the set of equations that forms the IBVP and the collection of terms of order up to ε. However, one should notice that this procedure does not solve the inconvenience that some of the boundary conditions, such as (4), (7) and (5), still must be applied in time-dependent surfaces. To overcome this problem, all the quantities of interest may be locally expanded by a Taylor's series around their mean positions and then substituted together with the Stokes expansions into the IBVP equations.

By following this procedure, the nonlinear free surface conditions are linearized and applied in time-invariant mean positions, as presented next:

1. Kinematic free surface condition

$$\frac{\partial\Phi^{(1)}}{\partial z} = -\frac{\partial\eta^{(1)}}{\partial t} \quad \text{on } z = 0. \tag{18}$$

2. Dynamic free surface condition

$$\eta^{(1)} = -\frac{1}{g}\frac{\partial\Phi^{(1)}}{\partial t} \quad \text{on } z = 0. \tag{19}$$

An analytic solution may be found by the boundary value problem defined by the Laplace's equation with the set of boundary conditions formed by the kinematic and dynamic boundary conditions. Considering scenarios of infinite water depth, for example, the incoming regular wave field potential is defined by the following expression:

$$\phi_{\mathrm{I}} = \frac{A_{\mathrm{I}}g}{\omega}e^{kz}\cos\left(kx - \omega t\right) \quad \text{on } z \leq 0, \tag{20}$$

which needs to satisfy the wave dispersion relation for infinite water depth:

$$k = \frac{\omega^2}{g}, \tag{21}$$

where A_{I}, ω and k are the incoming wave amplitude, angular frequency and number, respectively.

This solution is very useful when we are dealing with a linear theory description of the problem, because we may decompose the total potential Φ in a sum of a first-order disturbed wave field $\phi^{(1)}$ and the incoming regular wave field ϕ_{I}, avoiding then the necessity of using a numerical wave maker dispositive to simulate the later. Since ϕ_{I} is a known solution, we only need to include it in the zero-flux conditions accordingly.

From now on, the variable of the problem Φ will be changed by $\phi^{(1)}$ redefining also the set of boundary conditions that must be imposed. As ϕ_{I} satisfies the free surface conditions, these will be described by simply changing the variable Φ by $\phi^{(1)}$. For the other conditions, however, we will need to include the incoming wave potential as will be described in the next derivations.

Analogously to the free surface conditions, the floating body impermeability condition is also linearized and described by Eq. (22).

$$\nabla\phi^{(1)}\cdot\bar{\mathbf{n}}=\frac{\partial\boldsymbol{\delta}^{(1)}}{\partial t}\cdot\bar{\mathbf{n}}-\nabla\phi_{\mathrm{I}}\cdot\bar{\mathbf{n}}\quad\text{on }\bar{S}_{\mathrm{B}}.\tag{22}$$

In addition, the hydrodynamic forces/moments and the equations of motions should be calculated in a known body surface position, which is also part of the solution. This is overcome by assuming that the bodies' responses in waves are small, enabling the integration of the pressure field p on the body mean surface positions $\bar{S}_{\mathrm{B}}$. Moreover, since the pressure is determined by Bernoulli's equation (3), it also needs to be linearized to keep the formulation coherent with the linear theory presented so far. Thus, the first-order pressure, forces and moments on the body are calculated by Eqs. (23), (24) and (25), respectively:

$$p^{(1)}=-\rho\left(\frac{\partial\phi^{(1)}}{\partial t}+\frac{\partial\phi_{\mathrm{I}}}{\partial t}\right),\tag{23}$$

$$\mathbf{F}^{(1)}=\iint\limits_{\bar{S}_{\mathrm{B}}}-\rho\left(\frac{\partial\phi^{(1)}}{\partial t}+\frac{\partial\phi_{\mathrm{I}}}{\partial t}\right)\bar{\mathbf{n}}\,\mathrm{d}S,\tag{24}$$

$$\mathbf{M}_O^{(1)}=\iint\limits_{\bar{S}_{\mathrm{B}}}-\rho\left(\frac{\partial\phi^{(1)}}{\partial t}+\frac{\partial\phi_{\mathrm{I}}}{\partial t}\right)(\bar{\mathbf{r}}\times\bar{\mathbf{n}})\,\mathrm{d}S.\tag{25}$$

One should notice that the static term of the pressure was neglected in the previous equations, assuming that the body was initially at a state of equilibrium. However, if the body is shortly displaced from its initial position, restoring forces and moments appear, forcing the body to establish an equilibrium position again. For some degrees of freedom (normally heave, roll and pitch), these restoring forces and moments appear directly through the hydrostatic pressure integration; however, in some cases they need to be externally imposed, aiming at controlling the body horizontal offset around a mean position as, for example, in the case of a floating oil platform. In linear theory approach, restoring forces and moments may be shifted to the left side of equation (26) through the use of time-independent restoring coefficients. One last consideration is related to the lack of external damping coefficients which are sometimes necessary, since the potential flow theory does not account for viscous effects. Therefore, an external matrix of linear damping coefficients will be also considered, as can be observed in Eq. (26):

$$\mathbf{M}\frac{\partial^2\boldsymbol{\xi}^{(1)}}{\partial t^2}+\mathbf{C}\frac{\partial\boldsymbol{\xi}^{(1)}}{\partial t}+\mathbf{K}\boldsymbol{\xi}^{(1)}=\begin{pmatrix}\mathbf{F}^{(1)}\\ \mathbf{M}_O^{(1)}\end{pmatrix},\tag{26}$$

where $\mathbf{K}$ and $\mathbf{C}$ are 6×6 matrices containing the linear restoring and damping coefficients, respectively. The vector $\boldsymbol{\xi}^{(1)}=(\xi_1^{(1)},\xi_2^{(1)},\xi_3^{(1)},\xi_4^{(1)},\xi_5^{(1)},\xi_6^{(1)})$ contains the first-order motions for the six degrees of freedom, corresponding to surge, sway, heave, roll, pitch and yaw, respectively.

Special attention must be given for the linear pressure calculation expressed by (23), since we do not have an exact equation for the potential time derivative $\partial\phi^{(1)}/\partial t$. In fact, an erroneous choice of a numerical approximation for this term leads to unstable scheme for the time marching of the set of equations and, therefore, an adequate procedure must be chosen. In this work, we decided to apply the method presented by [10, 11], in which the pressure is evaluated directly using the acceleration potential (27), which can be written as the function of the velocity potential (28).

$$\mathbf{a}=\nabla\Psi\tag{27}$$

$$\Psi=\frac{\partial\phi}{\partial t}+\frac{1}{2}(\nabla\phi)^2.\tag{28}$$

In first order, the acceleration potential can be simplified to (29), which also respects Laplace's equation. Hence, another boundary value problem can be written for the acceleration potential. The body boundary condition can be defined by derivation in time of the body boundary condition for velocity potential (22), as can be seen in (30).

$$\Psi^{(1)}=\frac{\partial\phi^{(1)}}{\partial t},\tag{29}$$

$$\nabla\Psi^{(1)}\cdot\bar{\mathbf{n}}=\frac{\partial^2\boldsymbol{\delta}^{(1)}}{\partial t^2}\cdot\bar{\mathbf{n}}-\nabla\left(\frac{\partial\phi_{\mathrm{I}}}{\partial t}\right)\cdot\bar{\mathbf{n}}\quad\text{at}\quad\bar{S}_{\mathrm{B}}.\tag{30}$$

Furthermore, the free surface boundary condition is determined in terms of the dynamic free surface condition for the velocity potential, as presented in (31):

$$\Psi^{(1)}=-g\eta^{(1)}\quad\text{on }z=0.\tag{31}$$

Finally, the initial condition imposed is presented in (32):

$$\Psi^{(1)}=0\quad\text{on }t=0\text{ s}.\tag{32}$$

From now on, the superscript $^{(1)}$ denoting the first-order quantities of the formulation will be suppressed to simplify the notations.

2.2 Integral equations

The method adopted for solving the aforementioned problem is the boundary element method, developed by using Green's second identity (33), where $\partial\Omega'$ is the domain boundary and $\partial\Omega'_a$ is the boundary of a small sphere of radius a at a point (x,y,z) where the function G (Green's function) is singular.

$$\iint\limits_{\partial\Omega'} \left[\phi\frac{\partial G}{\partial n} - G\frac{\partial \phi}{\partial n}\right] \mathrm{d}\partial\Omega' = -\iint\limits_{\partial\Omega'_a} \left[\phi\frac{\partial G}{\partial n} - G\frac{\partial \phi}{\partial n}\right] \mathrm{d}\partial\Omega'. \tag{33}$$

There are several Green's functions available and already tested in the literature, see for instance [15, 16] and more recently [17]. In this work, we applied the Rankine sources (34), which are the fundamental solutions of Laplace's equation in polar coordinates. The use of Rankine source as the elementary singularity is mainly motivated by the resulting flexibility in the choice of the free surface conditions to be satisfied, which in the future may render the extension of the code for problems with forward speed and nonlinear flows problems:

$$G(P,Q) = \frac{1}{\sqrt{\left(x_p - x_q\right)^2 + \left(y_p - y_q\right)^2 + \left(z_p - z_q\right)^2}}. \tag{34}$$

Supposing that the domain contains only regular regions and analyzing the residue associated with the Rankine sources, the integral equation for the velocity potential can be summarized in (35), where P are field points and Q source points.

$$\iint\limits_{\partial\Omega'_{-P}} \left[\phi_Q\frac{\partial G_{PQ}}{\partial n_Q} - G_{PQ}\frac{\partial \phi_Q}{\partial n_Q}\right] \mathrm{d}\partial\Omega' = \begin{cases} -4\pi\phi_P & \text{if } P \text{ inside } \Omega' \\ -2\pi\phi_P & \text{if } P \text{ is at } \partial\Omega' \\ 0 \quad \text{if } P \text{ is outside } \Omega' \end{cases} \tag{35}$$

Analogously, the same procedure may be followed for the definition of an integral equation for the acceleration potential (36).

$$\iint\limits_{\partial\Omega'_{-P}} \left[\Psi_Q\frac{\partial G_{PQ}}{\partial n_Q} - G_{PQ}\frac{\partial \Psi_Q}{\partial n_Q}\right] \mathrm{d}\partial\Omega' = \begin{cases} -4\pi\Psi_P & \text{if } P \text{ inside } \Omega' \\ -2\pi\Psi_P & \text{if } P \text{ is at } \partial\Omega' \\ 0 \quad \text{if } P \text{ is outside } \Omega' \end{cases} \tag{36}$$

3 Numerical method

In a general description, the majority of the numerical algorithms which deal with the wave–body formulations in time domain solves the elliptical problem for the velocity and acceleration potential at a certain time step, whereas a time-marching scheme is used to update the boundary conditions to a new time step. In this work, the solution of the integral equations which compose the elliptical problem will be calculated by means of a boundary element method and the time-marching one will be performed by a fourth-order Runge–Kutta method (RK4).

3.1 Boundary element method

The boundary element method (panel method) is applied to solve the integral Eqs. (35) and (36). In this work we apply a low-order panel method which uses plane quadrilateral/triangular panels (surface elements) to discretize the surfaces and assume that the variable quantities are constant over each panel, simplifying reasonably the integration of the singularities. Reference [9], which was followed in this work, is considered a pioneering development in this topic, applying it to a wide variety of flow problems with bodies in infinite fluid.

With this approach, the boundary surfaces $\partial\Omega'$ are discretized in N_p plane quadrilateral/triangular panels, in which a unique point is selected to be a collocation point where the boundary conditions are imposed and the variable quantities are determined. It is quite obvious that the larger the number of panels, the better is the domain surface representation and also the assumption that the variable quantities are constant over each panel.

Therefore, we consider a sum of N_p integrals over separated surfaces $\partial\Omega'_j$ for all collocation points P, obtaining Eqs. (37) and (38) for the velocity and acceleration potential, respectively:

$$\begin{aligned} 2\pi\phi_{\mathrm{i}} + \sum_{j=1}^{N_p} \phi_j \iint\limits_{\partial\Omega'_j} \frac{\partial}{\partial n}\left(\frac{1}{r_{ij}}\right) \mathrm{d}\partial\Omega'_j \\ - \sum_{j=1}^{N_p} \frac{\partial\phi_j}{\partial n} \iint\limits_{\partial\Omega'_j} \frac{1}{r_{ij}} \mathrm{d}\partial\Omega'_j = 0 \quad i = 1 : N_p, \end{aligned} \tag{37}$$

$$\begin{aligned} 2\pi\Psi_{\mathrm{i}} + \sum_{j=1}^{N_p} \Psi_j \iint\limits_{\partial\Omega'_j} \frac{\partial}{\partial n}\left(\frac{1}{r_{ij}}\right) \mathrm{d}\partial\Omega'_j \\ - \sum_{j=1}^{N_p} \frac{\partial\Psi_j}{\partial n} \iint\limits_{\partial\Omega'_j} \frac{1}{r_{ij}} \mathrm{d}\partial\Omega'_j = 0 \quad i = 1 : N_p. \end{aligned} \tag{38}$$

In a more compact notation, Eqs. (37) and (38) may be replaced by Eqs. (39) and (40):

$$\sum_{j=1}^{N_p} \left[\phi_j D_{ij} - \frac{\partial\phi_j}{\partial n} S_{ij}\right] = -2\pi\phi_{\mathrm{i}} \quad i = 1 : N_p, \tag{39}$$

$$\sum_{j=1}^{N_p} \left[\Psi_j D_{ij} - \frac{\partial\Psi_j}{\partial n} S_{ij}\right] = -2\pi\Psi_{\mathrm{i}} \quad i = 1 : N_p, \tag{40}$$

where S_{ij} and D_{ij} are known in the literature as source and dipole influence coefficients, respectively.

In this method, a Neumman type condition is imposed on the submerged body surface to guarantee its impermeability condition. The choice of a boundary condition type to be imposed on the free surface is more flexible, since we can choose for Neumann or Dirichlet type. However, by applying a Neumman condition it is possible to realize that after the integral equation is solved, only the velocity potential ϕ would be known at all the boundary surfaces and an additional numerical spatial differentiation would be necessary to define the free surface elevation. To simplify the numerical method, we chose for a Dirichlet type, adopting the flux as variable in the free surface. Therefore, the potential ϕ is imposed, which allows the free surface conditions to be written as ordinary differential equations (ODEs).

Concluding, substitution of ϕ_j and Ψ_j for Dirichlet boundaries (i.e free surface) and $\partial\phi_j/\partial n$ and $\partial\Psi_j/\partial n$ for Neumann boundaries (i.e body surface, bottom etc.) results in two linear systems of N_p linear equations, which may be solved by simple matrix inversion.

3.2 Time integration

The time integral method is very important to ensure the accuracy and stability of the present numerical tool, which in practice leads to the application of higher-order schemes such as RK4, fifth-order Runge–Kutta–Gil method (RKG) and fourth-order Adams–Bashforth–Moulton (ABM). As stated by [12], the application of any of these methods to simulate problems involving ordinary waves and floating body motions provides substantial stability to the method. Therefore, following other authors such as [13, 14], we choose the RK4 method.

To update the boundary conditions of the IBVPs to a new time level, the time progressing is conducted by the integration of the kinematic and dynamic free surface conditions. In case of free floating bodies, the equations of motion must also be considered. These steps are followed until the desired simulation time T_s is reached. A summary of this procedure is presented in Fig. 2.

In the numerical scheme, the incident waves, velocities, accelerations, etc. are increased gradually using the ramp function $f_r(t)$ which guarantees a smooth and slow increase of the solution until the achievement of a steady state. The ramp function is defined by:

$$f_r(t) = \begin{cases} \frac{1}{2}\left[1 - \cos\left(\frac{\pi t}{T_r}\right)\right] & \text{if} \quad t \leq T_r, \\ 1 & \text{if} \quad t > T_r \end{cases} \tag{41}$$

where T_r is the ramp period which is normally set as a multiple of a characteristic wave period involved in the simulations.

3.3 Numerical damping zone

As mentioned before, the imposition of a radiation condition is mandatory to ensure a correct representation of a body floating in open sea, in which the incident, diffracted and irradiated waves cannot reflect back and influence the body motions again. In the ocean, this naturally occurs because the boundaries that could reflect part of the wave energy are usually far away and, then, the associated energy is dissipated by nonconservative forces or wave breaking.

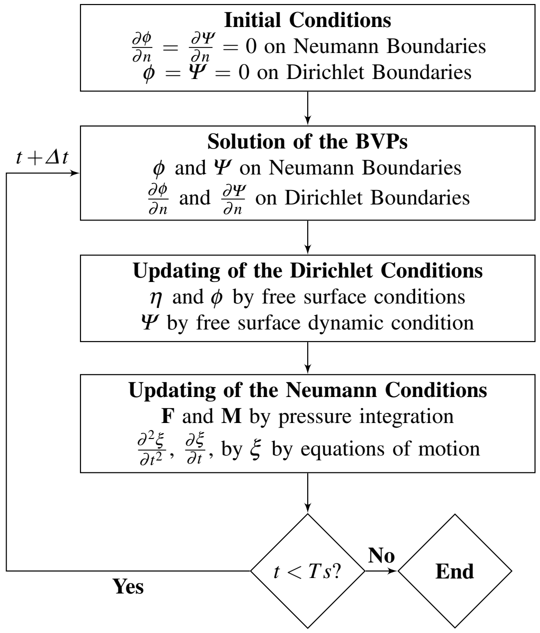

Fig. 2 Loop structure of the numerical method

In the experimental approach, there is always a beach or active absorbers to partially account for the dissipation or absorption of the waves, reducing the influence of reflect waves in the measurements of interest. The beach basic function, for example, is to dissipate the energy transported by the waves, but in a numerical simulation it is impossible to impose its physical behavior because all mathematical formulation is based on conservative fields and therefore no dissipation is expected.

Since computer memory is finite, we are then obliged to truncate the free surface somewhere and impose a numerical scheme in our model by the inclusion of a damping zone, which is also known as sponge boundary condition or numerical beach, first proposed by [18]. The relatively easy way of implementing leads to a widespread use of this condition, which is demonstrated by the vast quantity of works related to different approaches that we may find as, for example, [19–23].

In practice, this is performed by the inclusion of an energy dissipation term in the free surface boundary conditions, as follows:

$$\frac{\partial\eta}{\partial t} = \frac{\partial\phi}{\partial z} - \nu(x,y)\eta \quad \text{at} \quad z = 0$$
$$\text{and} \quad \sqrt{x^2 + y^2} > L_d z \tag{42}$$

$$\frac{\partial \phi}{\partial t} = -g\eta - \nu(x,y)\phi \quad \text{at} \quad z = 0$$
$$\text{and} \quad \sqrt{x^2 + y^2} > L_{\mathrm{d}}z, \tag{43}$$

in which $L_{\mathrm{d}}z$ is the distance from the global coordinate origin until the beginning of the damping region and $\nu(x, y)$ is a function that defines the dissipation of this region, described by:

$$\nu(x,y) = a\omega\left(\frac{\sqrt{x^2+y^2} - L_{\mathrm{d}}z}{b\lambda}\right)^2, \tag{44}$$

where a defines the intensity of dissipation and b the damping zone length. These values must be tuned by preliminary tests to avoid the occurrence of reflected waves which may spoil the solution. In general, we observe that the damping zone must have a minimum length of one wave length $b = 1$, whereas the intensity must be set in such a way that permits a progressive and smooth dissipation of the waves. Damping zones with large values of a (i.e $a \geq 3$) may behave as a fixed wall.

4 Numerical test cases

4.1 Verification of hydrodynamic load calculations

This section presents the computations of the hydrodynamic loads resulting from diffraction and radiation problems in infinite water depth, considering simple geometries as a hemisphere and a circular section cylinder. Benchmark results were obtained from calculations performed with the software WAMIT which solves the same boundary value problem defined here, but in the frequency domain. For the hemisphere radiation problem, the added mass and potential damping coefficients are compared to the closed solutions presented by [24].

The hemisphere surface of unitary radius $r_{\mathrm{h}} = 1$ m was discretized in three different grids with 200, 800 and 3200 panels and the circular section cylinder of radius $r_{\mathrm{c}} = 1$ m and draught $T_{\mathrm{c}} = 1$ m, in 120, 500 and 2000 panels. In the cylinder case, the panels are more concentrated near the intersection region formed by the encountering of the free surface and the body surface. This was done to guarantee a minimum resolution of panels for cases involving high-frequency waves in which their lengths are small and the velocity profiles are confined to this region. In fact, as observed by [9], if several small elements are in the vicinity of a larger one, the accuracy of the solution is associated with the larger elements. For the hemisphere, this was guaranteed by increasing the total number of panels. The six body meshes considered in the calculations are displayed in Fig. 3.

The free surface length depends directly on the wavelengths that will be simulated. For these computations, we considered circular free surfaces meshes with radius $r_{\mathrm{fs}} = 30$ m, providing sufficient space for most of the waves herein considered. As well as the body surfaces, three different panel meshes are considered containing 289,

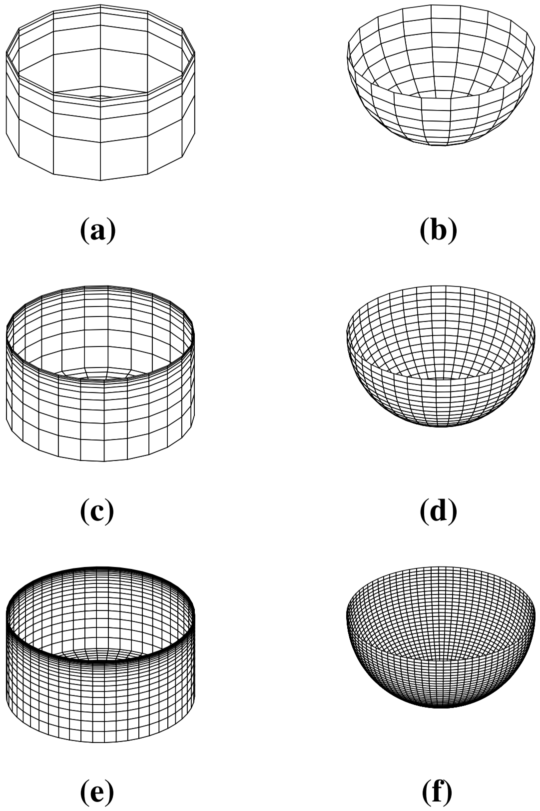

Fig. 3 Cylinder and hemisphere panel meshes used in the computations. **a**, **c**, **e** 120, 500 and 2000 cylinder panel meshes, respectively. **b**, **d**, **f** 200, 800 and 3200 hemisphere panel meshes, respectively

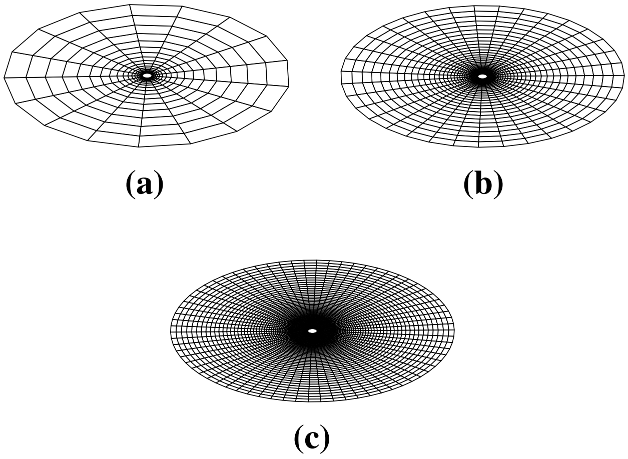

Fig. 4 Free surface panel meshes used in the computations. **a**–**c** refer to the 289, 1225 and 4900 free surface panel meshes, respectively

Table 1 Main numbers of the panel meshes used in the computations

	Hemisphere			Cylinder		
	Coarse	Medium	Fine	Coarse	Medium	Fine
Body mesh	200	800	3200	120	500	2000
Free surface mesh	289	1225	4900	289	1225	4900
Final mesh	489	2025	8100	409	1725	6900

Table 2 Regular incoming waves used in simulations

ID	ω (rad/s)	T (s)	λ (m)	ID	ω (rad/s)	T (s)	λ (m)
1	1.716	3.662	20.932	13	4.429	1.419	3.142
2	1.981	3.172	15.707	14	4.952	1.269	2.514
3	2.215	2.837	12.563	15	5.425	1.158	2.094
4	2.426	2.590	10.473	16	5.860	1.072	1.795
5	2.620	2.398	8.979	17	6.264	1.003	1.571
6	2.801	2.243	7.856	18	6.644	0.946	1.396
7	2.971	2.115	6.983	19	7.004	0.897	1.256
8	3.132	2.006	6.284	20	7.672	0.819	1.047
9	3.431	1.831	5.236	21	8.287	0.758	0.898
10	3.706	1.695	4.488	22	8.859	0.709	0.785
11	3.962	1.586	3.927	23	9.396	0.669	0.698
12	4.202	1.495	3.491	24	9.905	0.634	0.628

1225 and 4900 panels. Figure 4 displays the meshes used in the computations, where it is possible to observe that a high number of panels are concentrated near the body surface.

A set of six panel meshes is then constructed by grouping the body and free surface meshes in pairs. Denoting the meshes with the lowest number of panels as coarse meshes, the intermediates as medium meshes and the one with greatest resolution as fine mesh, Table 1 presents the main numbers of the panel meshes that will be simulated.

We begin our numerical result presentation, simulating cases of fixed bodies under the action of incoming regular waves. Table 2 presents the main features of the set of 24 regular waves in a frequency range between 1.716 and 9.905 rad/s, which were tested in our numerical model. All the waves present unitary amplitudes $A_\mathrm{I} = 1$ m. For all the simulations, the time step was set to $\Delta t = T/60$ s and the numerical beach coefficients were set to $a = 1$ and $b = 1$, with these parameters being defined after a convergence analysis [25].

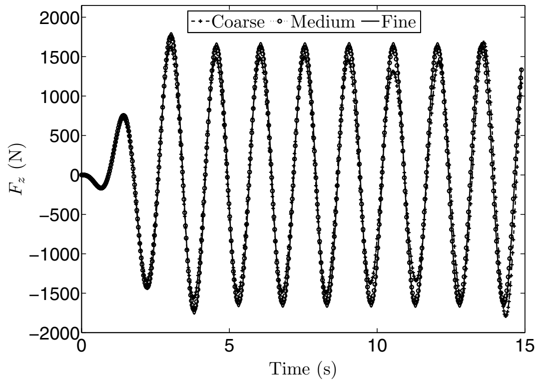

Fig. 5 Hydrodynamic vertical force F_z induced by a wave with frequency of $\omega = 4.202$ rad/s for cylinder body

Figures 5, 6 and 7 present the time series of the vertical hydrodynamic forces F_z obtained for each one of the panel meshes, considering incoming waves of frequencies $\omega = 4.202$ rad/s, $\omega = 6.264$ rad/s and $\omega = 9.905$ rad/s, respectively. It is possible to realize that as the angular frequency increases, larger differences in terms of amplitude and phase between the forces calculated with the different meshes are observed. Amplitude modulations are clearly observed for the coarse mesh when simulating waves with frequency higher than $\omega = 6.264$ rad/s. This may be explained by the insufficient number of panels per wavelength that is required to correctly satisfy the dispersion relation of waves in infinite water depth. For the highest frequency, for example, the vertical forces calculated by the coarse mesh present nonphysical results with order of magnitude much larger than those obtained with the other meshes. Moreover, for this frequency we may also observe variations of phase calculated when using each of the considered panel meshes. Results for the medium and fine meshes present better agreement for all the frequencies, but for the highest one, indicating that only the fine mesh is capable of correctly propagating waves of such small length. The results for the hemisphere body are not presented, since the same behavior was observed. This was expected,

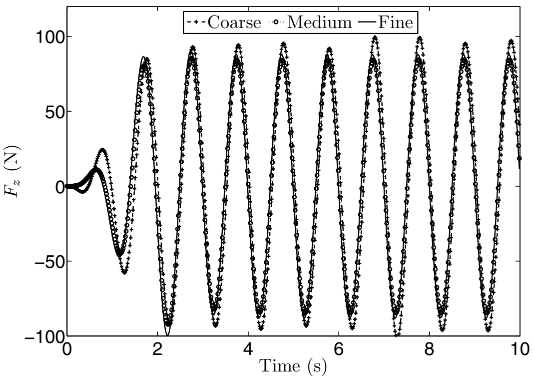

Fig. 6 Hydrodynamic vertical force F_z induced by a wave with frequency of $\omega = 6.264$ rad/s for cylinder body

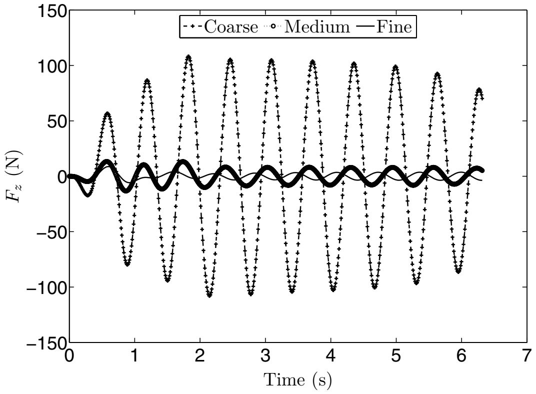

Fig. 7 Hydrodynamic vertical force F_z induced by a wave with frequency of $\omega = 9.905$ rad/s for cylinder body

since the propagation of waves is related to the free surface meshes which are the same for both body geometries.

To check the convergence of the results, we compare the horizontal and vertical non-dimensional forces for all panel meshes and wave frequencies presented in Table 2. For the cylinder, the non-dimensional moment M_y around the y-axis is also presented.

The non-dimensional forces and moments are calculated by:

$$\begin{array}{ll} \text{Hemisphere} & \text{Cylinder} \\ \bar{F}_x = \frac{f_x}{\frac{2}{3}\pi r_{\mathrm{h}}^3 \rho g} & \bar{F}_x = \dfrac{f_x}{\rho g \pi r_{\mathrm{c}}^2 T_{\mathrm{c}}} \\ \bar{F}_z = \frac{f_z}{\frac{2}{3}\pi r_{\mathrm{h}}^3 \rho g} & \bar{F}_z = \dfrac{f_z}{\rho g \pi r_{\mathrm{c}}^2 T_{\mathrm{c}}} \\ & \bar{M}_y = \frac{m_y}{\rho g \pi r_{\mathrm{c}}^3 T_{\mathrm{c}}} \end{array} \tag{45}$$

where f_x, f_z and m_y are the amplitudes of the forces F_x and F_z and moment M_y, respectively.

The convergence analysis for the non-dimensional horizontal and vertical hydrodynamic forces for the hemisphere body is presented in Figs. 8 and 9, respectively. As expected, deviations among the meshes tend to be more pronounced for the highest frequencies, where a very refined free surface mesh becomes essential for an accurate calculation of the diffraction wave fields. In a general view, the present values recovered very well the values calculated by the WAMIT higher-order scheme.

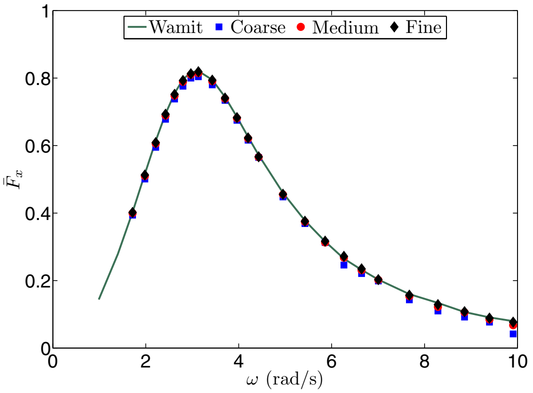

Fig. 8 Convergence analysis of the non-dimensional horizontal hydrodynamic force $\bar{F}_x$ for the hemisphere body and comparison with *Wamit* data

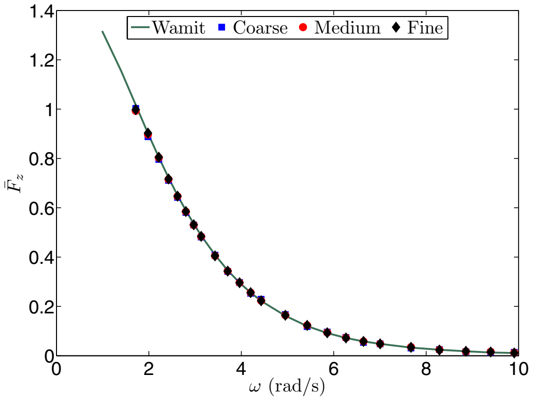

Fig. 9 Convergence analysis of the non-dimensional vertical hydrodynamic force $\bar{F}_z$ for the hemisphere body and comparison with *Wamit* data

The simulations with the cylinder presented very similar trends in comparison to the hemisphere ones. Again, convergence of the results is confirmed increasing the number of panels and very low relative errors are observed for the majority of wave frequencies. Once more, the data are illustrated in Figs. 10, 11 and 12. Again, a good agreement between the WAMIT results and the present calculations is observed.

Next, we present the simulations of forced harmonic oscillations imposed on both the hemisphere and cylinder body. In contrast to fixed body simulations, this study does not contain incident waves and the hydrodynamic loads are generated only by body motions with unitary amplitude. Again, all the simulations were run with a time step of $\Delta t = T/60$ s.

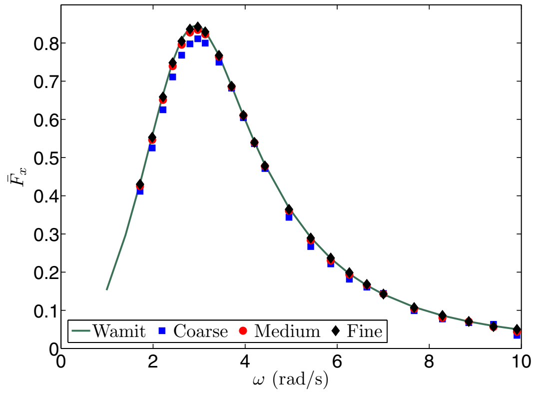

Fig. 10 Convergence analysis of the non-dimensional horizontal hydrodynamic force $\bar{F}_x$ for the cylinder body and comparison with *Wamit* data

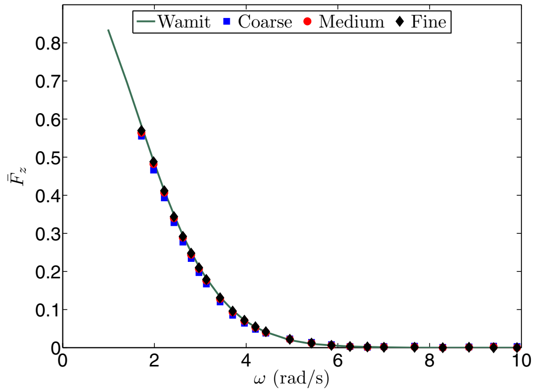

Fig. 11 Convergence analysis of the non-dimensional vertical hydrodynamic force $\bar{F}_z$ for the cylinder body and comparison with *Wamit* data

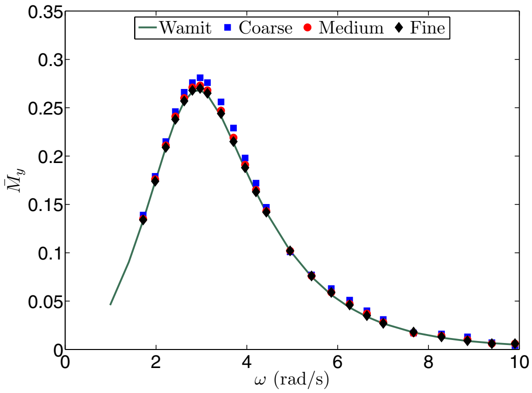

Fig. 12 Convergence analysis of the non-dimensional hydrodynamic moment $\bar{M}_y$ for the cylinder body and comparison with *Wamit* data

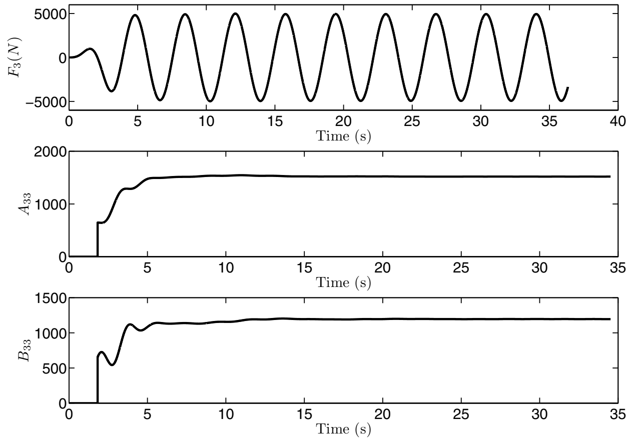

Fig. 13 Determination of A_{33} and B_{33} coefficients

In wave linear theory, it is quite usual to decompose the total hydrodynamic force induced by harmonic oscillations in two different components denoted by added mass and radiation damping, which are in phase with the body acceleration and velocity, respectively.

A time series example of vertical force obtained with a pure heave forced motion simulation considering the hemisphere body (fine mesh) is presented in Fig. 13. Moreover, the figure also presents moving window Fourier analyses of the signal, which provide the time traces for the added mass A_{33} and radiation damping B_{33}. Notice that the coefficient curves present some oscillations at the beginning of the simulation, alerting us that the hydrodynamic forces are still in a transient period. Going further, we observe that after a certain instant of time, the signals become practically constant, indicating that the force is in steady state. After a constant behavior of the curve is observed, the added mass and radiation damping coefficients are then determined by an average of its values.

The calculations of the added mass and radiation damping coefficients are then repeated using the same angular frequencies described in Table 2. Convergence analysis of the results are performed simulating each case for the coarse, medium and fine mesh presented in Table 1. Aiming at verifying the results, the coefficients obtained with the hemisphere body are compared to the analytical solution presented by [24], whereas the ones for the cylinder body are compared to data calculated by the software WAMIT. The non-dimensional added mass and radiation damping coefficients $\bar{A}_{ij}$ and $\bar{B}_{ij}$ are determined by:

$$\begin{array}{llll}
\text{Hemisphere} & \text{Cylinder} & & \\
\bar{A}_{ij}=\dfrac{A_{ij}}{\frac{2}{3}\pi r_{\mathrm{h}}^{3}\rho} & \bar{A}_{ij}=\dfrac{A_{ij}}{\rho\pi r_{\mathrm{c}}^{2}T_{\mathrm{c}}} & \text{for} & i,j\leq 3 \\
\bar{B}_{ij}=\dfrac{B_{ij}}{\frac{2}{3}\pi r_{\mathrm{h}}^{3}\rho\omega} & \bar{B}_{ij}=\dfrac{B_{ij}}{\rho\pi r_{\mathrm{c}}^{2}T_{\mathrm{c}}\omega} & \text{for} & i,j\leq 3 \\
 & \bar{A}_{ij}=\dfrac{A_{ij}}{\rho\pi r_{\mathrm{c}}^{3}T_{\mathrm{c}}} & \text{for} & i,j\geq 4 \\
 & \bar{B}_{ij}=\dfrac{B_{ij}}{\rho\pi r_{\mathrm{c}}^{3}T_{\mathrm{c}}\omega} & \text{for} & i,j\leq 4.
\end{array} \qquad (46)$$

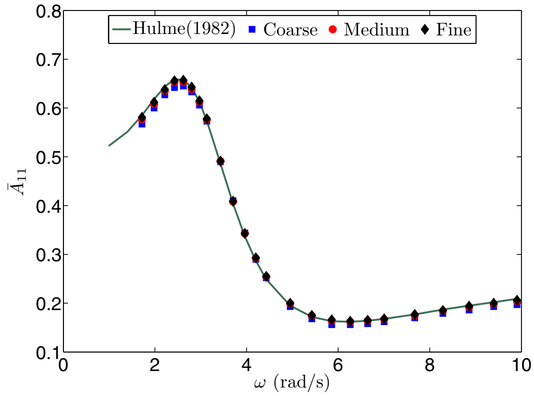

Fig. 14 Convergence analysis of the added mass coefficient $\bar{A}_{11}$ for the hemisphere body and comparison with data obtained in reference [24]

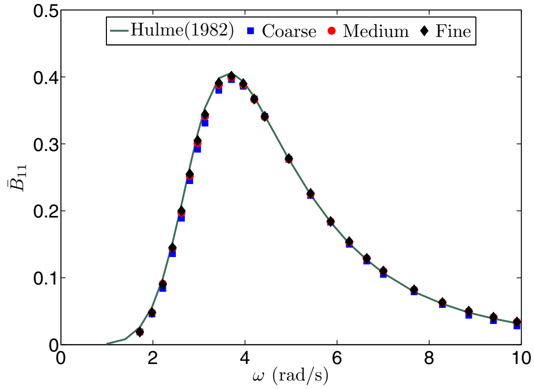

Fig. 15 Convergence analysis of the radiation damping coefficient $\bar{B}_{11}$ for the hemisphere body and comparison with data obtained in reference [24]

The non-dimensional added mass and radiation damping coefficients for heave and surge modes of the hemisphere body are presented in Figs. 14, 15, 16 and 17. Notice that the present calculations agree very well with the analytical solutions derived by [24] for all the analyzed angular frequencies. In addition, differences between the results obtained with each panel mesh are very small, pointing out that for this body geometry very low computational costs are necessary for a reasonable numerical prediction of these coefficients.

The same trend is not observed in the cylinder results, displayed in the Figs. 18, 19, 20 and 21. Although fine results are observed for the medium and fine meshes, calculations performed with the coarse mesh do not provide accurate results as, for example, for the added mass coefficients for the heave mode presented in Fig. 20. Looking

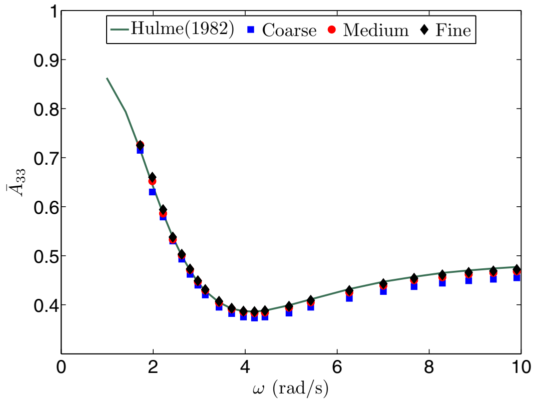

Fig. 16 Convergence analysis of the added mass coefficient $\bar{A}_{33}$ for the hemisphere body and comparison with data obtained in reference [24]

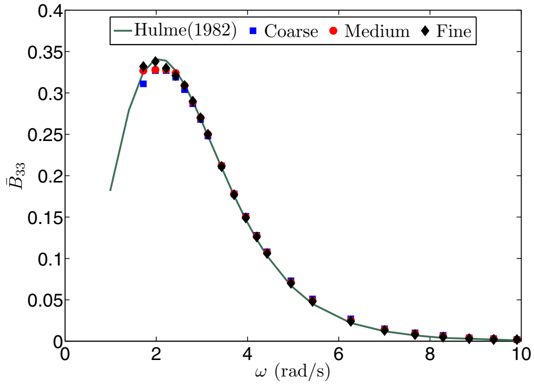

Fig. 17 Convergence analysis of the radiation damping coefficient $\bar{B}_{33}$ for the hemisphere body and comparison with data obtained in reference [24]

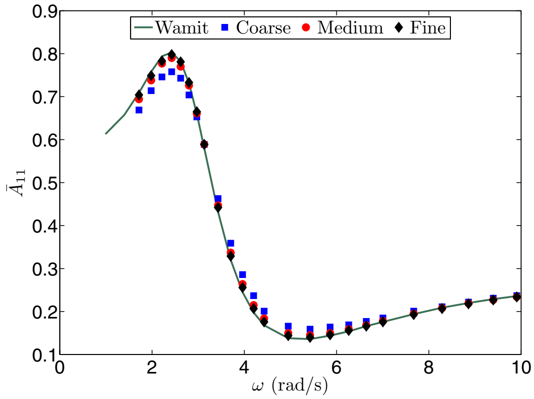

Fig. 18 Convergence analysis of the added mass coefficient $\bar{A}_{11}$ for the cylinder body

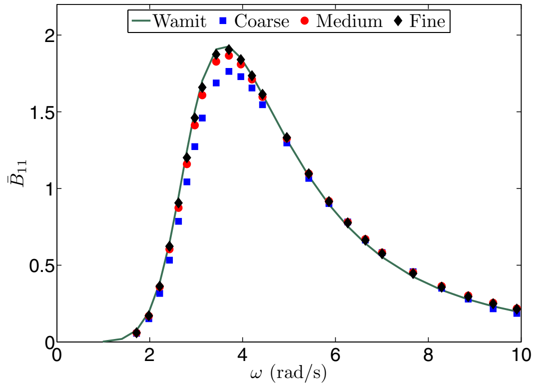

Fig. 19 Convergence analysis of the radiation damping coefficient $\bar{B}_{11}$ for the cylinder body

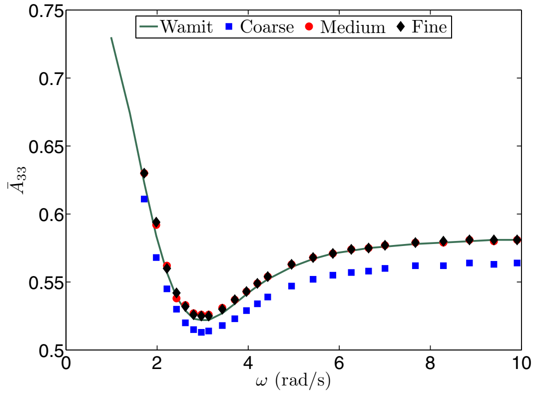

Fig. 20 Convergence analysis of the added mass coefficient $\bar{A}_{33}$ for the cylinder body

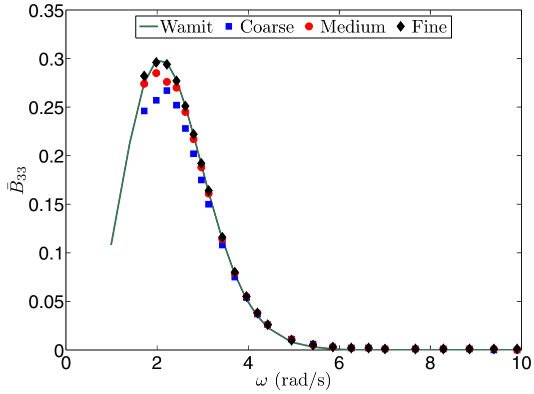

Fig. 21 Convergence analysis of the radiation damping coefficient $\bar{B}_{33}$ for the cylinder body

for the pitch mode coefficients $\bar{A}_{55}$ and $\bar{B}_{55}$, we conclude that even the fine mesh is insufficient to accurately predict the same values calculated by the WAMIT higher-order scheme and, therefore, highest panel resolutions should be applied (Figs. 22, 23).

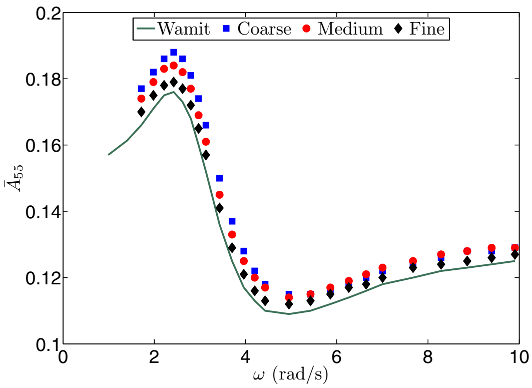

Fig. 22 Convergence analysis of the added mass coefficient $\bar{A}_{55}$ for the cylinder body

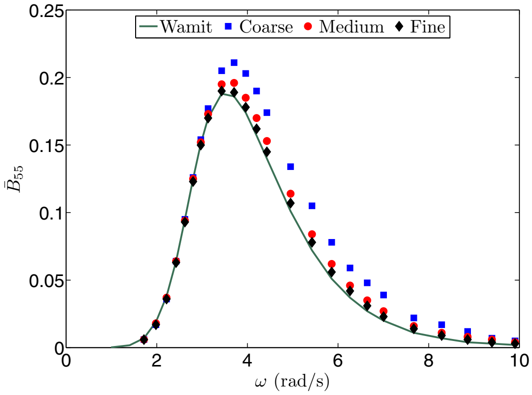

Fig. 23 Convergence analysis of the radiation damping coefficient $\bar{B}_{55}$ for the cylinder body

4.2 Free floating simulations

The results presented so far still did not involve calculations considering the body equations of motions coupled with the integral equations derived from the hydrodynamic problem and, therefore, we cannot conclude whether the coupling scheme, previously proposed by [10, 11], is implemented correctly or not. In this sense, we apply our numerical code for the evaluation of free motions of hemisphere and cylinder bodies. The calculations are performed with the panel meshes presented in Table 1. In the simulations, the incident regular waves with unitary amplitude $A_I = 1$ m propagate in x positive direction with the angular frequencies presented in Table 2. Again, the time step and the numerical beach zone coefficients were set to $\Delta t = T/60$ s, $a = 1$ and $b = 1$, respectively.

Table 3 Principal characteristics of the cylinder and hemisphere and settings of the simulations

Parameters	Cylinder	Hemisphere
Radius (m)	1.00	1.00
Draught (m)	1.00	1.00
Mass (kg)	3.14E+3	2.09E+3
Pitch inertia[a] (kg m^2)	1.57E+3	–
COG X coordinate[b] (m)	0.00	0.00
COG Y coordinate[b] (m)	0.00	0.00
COG Z coordinate[b] (m)	−0.50	−0.50
C55 (kg m^2/s)	4.35E+2	–

[a] Values were calculated in relation to the body center of gravity

[b] Values are described in relation to the global coordinate system $(x, y, z) = (0, 0, 0)$

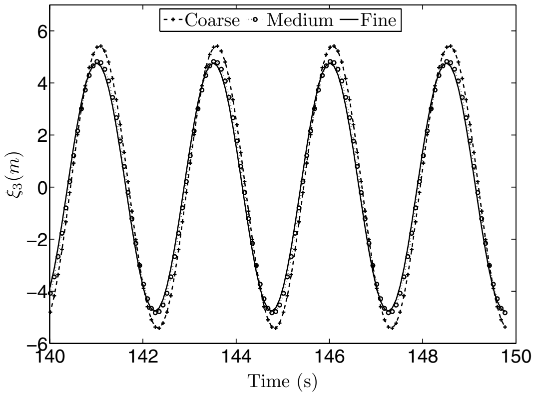

Fig. 24 Time history of the cylinder heave motion for the coarse, medium and fine meshes. Incoming wave with angular frequency $\omega = 2.51$ rad/s

For the calculation of the body motions in waves, we also had to define matrices of mass/inertias for each of the geometries evaluated. Moreover, for the calculations involving the cylinder, in which the pitch D.O.F was also evaluated, the linear external damping coefficient C_{55} was also considered to account for viscous effects neglected in our model. The main parameters considered in the simulations are presented in Table 3.

Typical time histories of the cylinder and hemisphere heave motions are exemplified in Figs. 24 and 25, respectively. These simulations were carried out with incoming waves with frequencies equal to the heave natural frequencies of each body. For a better visualization of the curves, only a part of the steady-state portion of the signals are presented. It is worth mentioning that the time histories presented a regular behavior, even simulating the body responses for more than a 100 wave cycles, demonstrating the stability of the code. In fact, the simulation could be continued for much more time, maintaining the quality of the results.

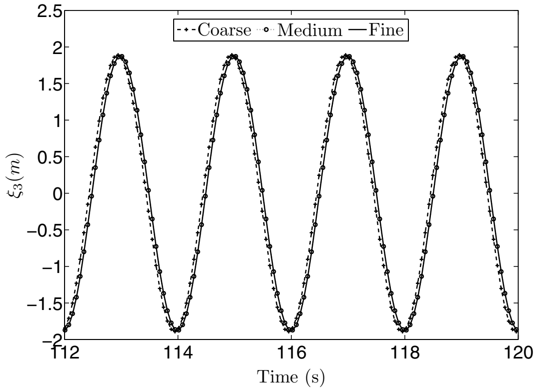

Fig. 25 Time history of the hemisphere heave motion for the coarse, medium and fine meshes. Incoming wave with angular frequency $\omega = 3.13$ rad/s

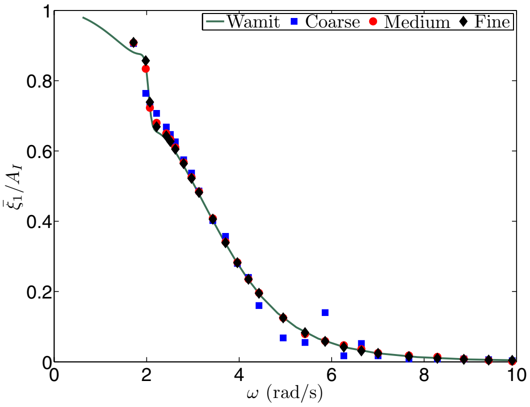

Fig. 26 Convergence analysis of the cylinder surge RAO and comparison with *Wamit* data

The convergence of the bodies' motion results for each one of the wave frequencies described in Table 2 is evaluated next. Furthermore, the results are compared with data provided by the software WAMIT. This evaluation is done in the frequency domain by calculating the motions of RAOs by a fast Fourier transform (FFT) analysis on the steady-state portion of each motion time series.

The cylinder RAOS of surge, heave and pitch motions obtained with the present method and WAMIT are plotted in Figs. 26, 27 and 28, respectively. Overall, a good agreement is observed with the WAMIT results. As can be seen, the results converge with the increasing of the number of panels, which is demonstrated by very similar results obtained with the medium and fine meshes. Notice, however, that by applying the coarse mesh, the curves tend to present an oscillatory behavior, which is intensified with the increase in the wave frequency. As discussed before, this occurs due to the low resolution of panels per wavelength, which causes the appearance of an amplitude modulation in the signal.

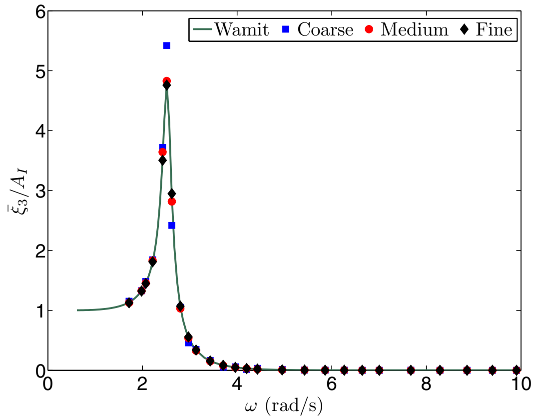

Fig. 27 Convergence analysis of the cylinder heave RAO and comparison with *Wamit* data

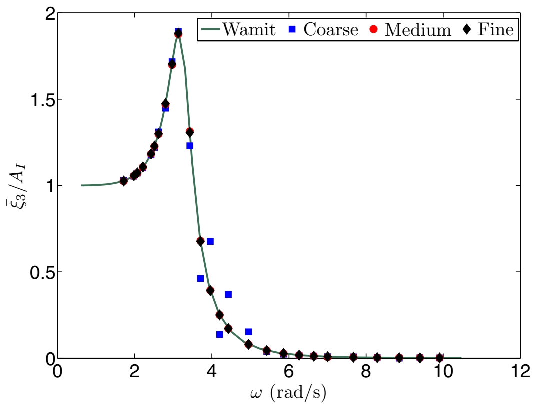

Fig. 30 Convergence analysis of the sphere heave RAO and comparison with *Wamit* data

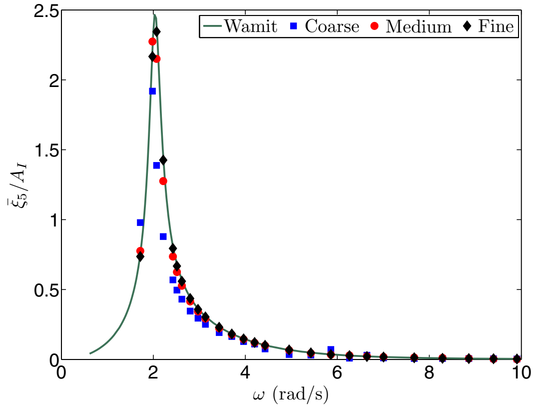

Fig. 28 Convergence analysis of the cylinder pitch RAO and comparison with *Wamit* data

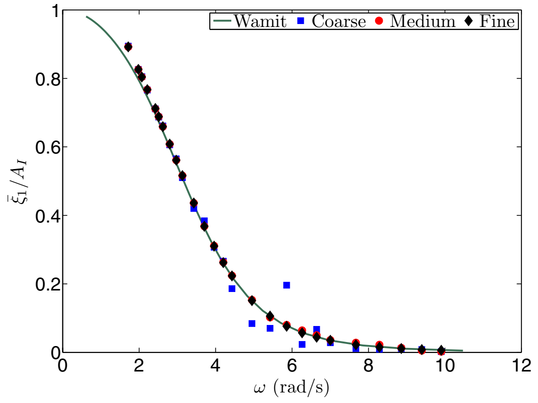

Fig. 29 Convergence analysis of the sphere surge RAO and comparison with *Wamit* data

The analogous results for the hemisphere body are presented in Figs. 29 and 30 for surge and heave motions, respectively. In general, the same conclusions pointed out for the cylinder are maintained, in which the medium and fine mesh results agreed very well with the WAMIT data. Furthermore, these results demonstrate the capability of our code to predict the motions of floating bodies in waves, confirming that the second integral equation defined for the acceleration potential was correctly implemented and the equilibrium between the dynamic and hydrodynamic forces was conserved during the whole simulation.

5 Free floating simulations with an FPSO

Numerical simulations are now conducted to a converted FPSO VLCC hull type. The results are compared to experimental data obtained in wave tests carried out at the CH-TPN-USP, in Sao Paulo, Brazil, which is a wave basin with dimensions of 14 m×14 m and water depth of 4 m. This tank is equipped with a set of 148 independent flaps for the generation and active absorption of waves, which provides great precision and stability to the wave field during the experimental measurements; see for instance [26]. A perspective view of the wave basin is illustrated in Fig. 31.

For the execution of the tests, a 1:90 small-scale model of the VLCC hull was positioned at the middle of the tank and equipped with reflective targets used by an optical tracking system which was mounted on the carriage for the measurement of 6 D.O.F model motions. In addition, a set of four soft springs was attached to the model and fixed to four vertical bars positioned at the corners of the wave basin to control its horizontal displacements. The equivalent restoring coefficient in the horizontal plane was determined by pullout tests. As the main goal of the tests was the study of roll motions, only beam waves were considered in the test matrix, which included regular, transient

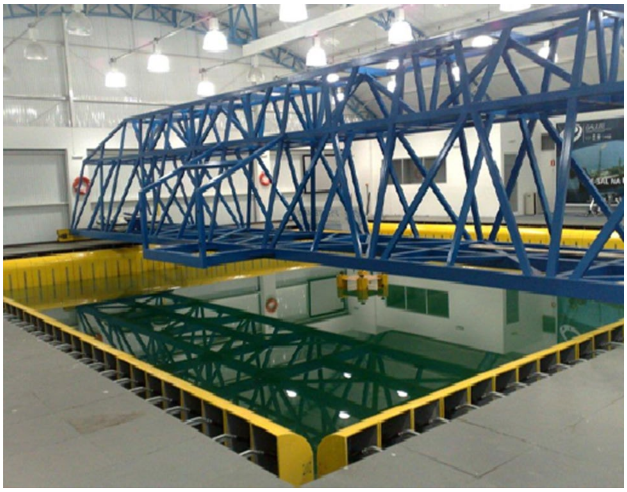

Fig. 31 Hydrodynamic calibrator of the numerical offshore tank on the University of Sao Paulo (CH-TPN-USP)

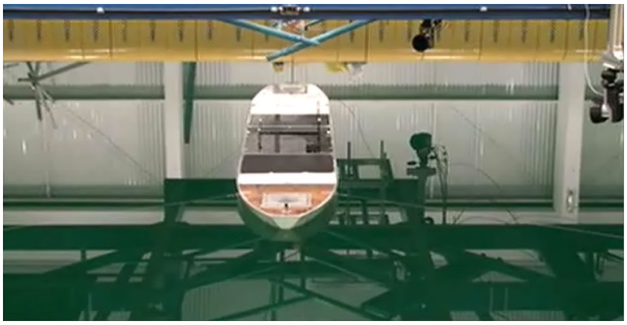

Fig. 32 Hydrodynamic calibrator of the numerical offshore tank in the University of Sao Paulo (CH-TPN-USP)

and sea wave conditions. Figure 32 presents a view of the model during the tests.

Concerning the regular waves, a study increasing the incoming wave amplitude for a fixed wave frequency $\omega_I = 0.443$ rad/s (near the roll resonance frequency) was conducted aiming at investigating the nonlinear roll motion response and its associated damping coefficients. For this study, however, only the regular wave of smallest steepness will be considered, in accordance with the linear wave theory considered here. The transient wave, in turn, was used for a fast RAO determination, in which a wave package with a constant amplitude of 3 m, in full scale, and frequencies between 0.349 and 0.785 rad/s was applied. In this wave package, the maximum wave steepness was around 3 %, being also within the scope of the linear wave theory. By now, the irregular waves were not used for comparison purposes.

The main characteristics of the FPSO model (in full scale) are listed in Table 4. Model center of gravity and inertia of roll, pitch and yaw were calibrated using ballast weights.

Table 4 Principal characteristics of the FPSO VLCC hull and the settings of the simulations

Length over all	334.44 (m)
Beam moulded	54.72 (m)
Depth moulded	21.51 (m)
Draught	21.51 (m)
Mass	3.09E+08 (kg)
Roll inertia[a]	1.05+11 (kg m^2)
Pitch inertia[a]	1.79E+12 kg m^2
Yaw inertia[a]	1.83E+12 kg m^2
COG X coordinate[b]	10.10 (m)
COG Y coordinate[b]	0.00 (m)
COG Z coordinate[b]	−6.76 (m)
K22	8.67E+05 (kg/s)
C44 (5 % C_{crit})	5.48E+09 (kg m/s)
C44 (6 % C_{crit})	6.03E+09 (kg m/s)

[a] Values were calculated in relation to the body center of gravity

[b] Values are described in relation to the global coordinate system $(x, y, z) = (0, 0, 0)$

The numerical simulations for the RAO determination were conducted considering a set of 44 regular waves, which covered a frequency range between 0.307 and 0.873 rad/s, as observed in Table 5. As viscous damping effects may not be neglected when evaluating roll motions, the numerical results are presented for two different external roll damping coefficients $C44$, also presented in Table 4, which were calculated as 5 and 6 % of the critical damping C_{crit}.

The FPSO VLCC body and the free surface mesh used in the simulations are illustrated in Figs. 33 and 34, respectively. The meshes designed for the FPSO and the free surface were defined after a convergence test and resulted in 1088 and 3600 panels, respectively. The free surface mesh was constructed with radius $r_{\text{fs}} = 2000$ m and with a highest panel concentration near the FPSO position. Once more, the time step was set to $\Delta t = T/60$ s and the damping zone coefficients to $b = 1$ and $a = 1$.

Figures 35, 36 and 37 present the comparisons between numerical results and experimental data for sway, heave and roll D.O.F., respectively. As expected, the change of the external roll damping coefficients brought higher deviations at frequencies near the FPSO roll natural frequency. In addition, this variation did not influence the heave motions and slightly impacted the sway motions, which is justified by the existence of a nonzero hydrodynamic cross term coefficient relating these two D.O.F. In general, the numerical method recovered well the experimental curves for sway and heave D.O.F., being capable of predicting the motion amplitudes reasonably well, mainly if we consider the presence of uncontrolled uncertainties inherent to

Table 5 Regular incoming waves used in the FPSO VLCC hull simulations

ID	ω (rad/s)	T (s)	λ (m)	ID	ω (rad/s)	T (s)	λ (m)
1	0.307	20.466	653.992	23	0.517	12.153	230.605
2	0.323	19.453	590.805	24	0.534	11.766	216.156
3	0.340	18.480	533.201	25	0.550	11.424	203.762
4	0.356	17.649	486.350	26	0.566	11.101	192.405
5	0.372	16.890	445.413	27	0.582	10.796	181.971
6	0.388	16.194	409.435	28	0.598	10.507	172.364
7	0.390	16.111	405.247	29	0.614	10.233	163.498
8	0.395	15.907	395.052	30	0.631	9.958	154.807
9	0.400	15.708	385.238	31	0.647	9.711	147.245
10	0.404	15.552	377.647	32	0.663	9.477	140.224
11	0.405	15.514	375.784	33	0.679	9.254	133.693
12	0.415	15.140	357.893	34	0.695	9.041	127.608
13	0.420	14.960	349.422	35	0.711	8.837	121.930
14	0.425	14.784	341.249	36	0.728	8.631	116.302
15	0.430	14.612	333.359	37	0.744	8.445	111.353
16	0.435	14.444	325.739	38	0.760	8.267	106.714
17	0.437	14.378	322.765	39	0.776	8.097	102.359
18	0.443	14.183	314.081	40	0.792	7.933	98.265
19	0.453	13.870	300.367	41	0.808	7.776	94.412
20	0.469	13.397	280.223	42	0.825	7.616	90.561
21	0.485	12.955	262.039	43	0.841	7.471	87.148
22	0.501	12.541	245.569	44	0.857	7.332	83.924
				45	0.873	7.197	80.876

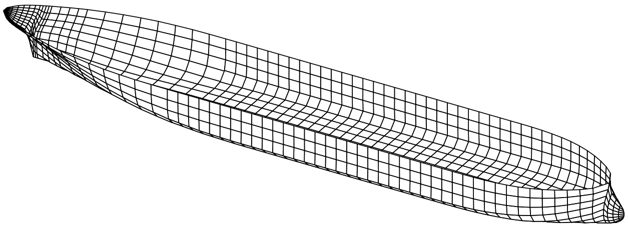

Fig. 33 FPSO VLCC hull panel mesh

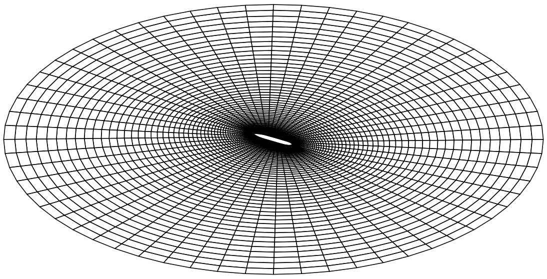

Fig. 34 Free surface panel mesh for the FPSO VLCC simulations

the model test, such as small model geometry errors and its calibration parameters, as well as slight differences in the horizontal restoration coefficient input in the simulation and also the linearization hypothesis established by our linear numerical model.

Direct comparisons between numerical and experimental motion time series for sway (ξ_2), heave (ξ_3) and roll (ξ_4) are presented in Fig. 38, considering $C_{44} = 0.05C_{\text{crit}}$, and in Figure 39 for $C_{44} = 0.06C_{\text{crit}}$. These motions are results of the FPSO interaction with a regular wave of frequency $\omega = 0.443$ rad/s and amplitude $A_{\text{I}} = 0.92$ m, both in full scale. The time series are synchronized considering only the motion data of one D.O.F. (sway) so as to preserve the phase information with the other D.O.F. A good agreement is observed for the heave motion time series, in which the experimental and numerical curves are practically equal. On the other hand, although the roll and sway motion phases were predicted accurately, small discrepancies in amplitude may be noticed, especially in Fig. 39, where an external coefficient of $C_{44} = 0.06C_{\text{crit}}$ was applied. This result is contradictory to the comparisons made for the roll RAO, see Fig. 37, obtained with the transient wave, in which the consideration of the higher damping coefficient clearly improved the curves' agreement. However, as could also be observed in the figure, the roll RAO measured in the

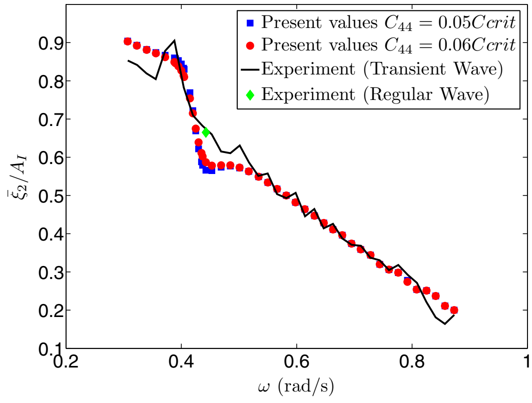

Fig. 35 Comparison between numerical results and experimental data of sway response amplitude operator for the FPSO VLCC hull

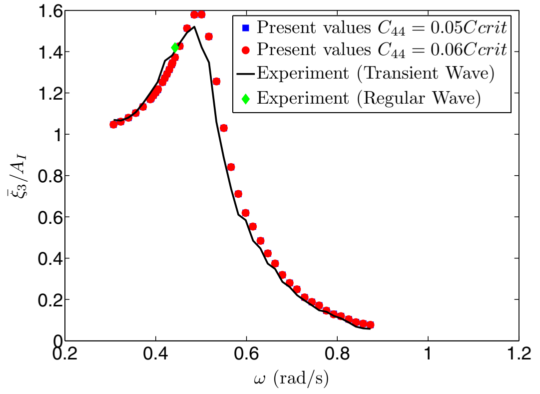

Fig. 36 Comparison between numerical results and experimental data of heave response amplitude operator for the FPSO VLCC hull

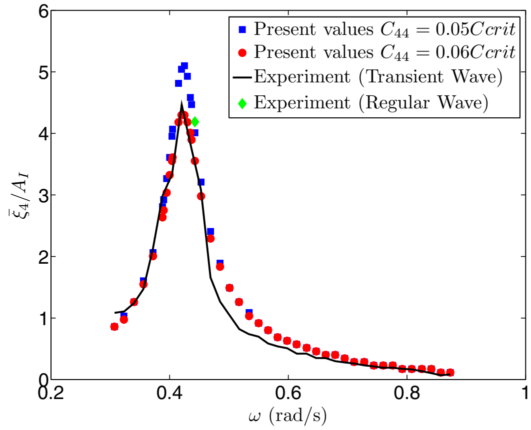

Fig. 37 Comparison between numerical results and experimental data of roll response amplitude operator for the FPSO VLCC hull

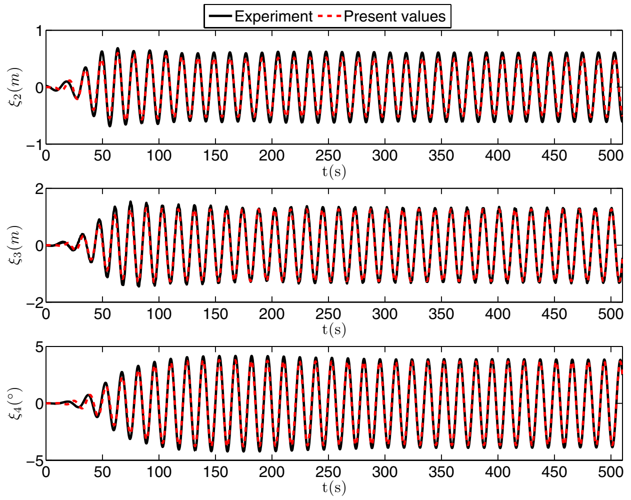

Fig. 38 Comparison between numerical and experimental motion time series for sway (ξ_2), heave (ξ_3) and roll (ξ_4), considering $C_{44} = 0.05C_{\mathrm{crit}}$

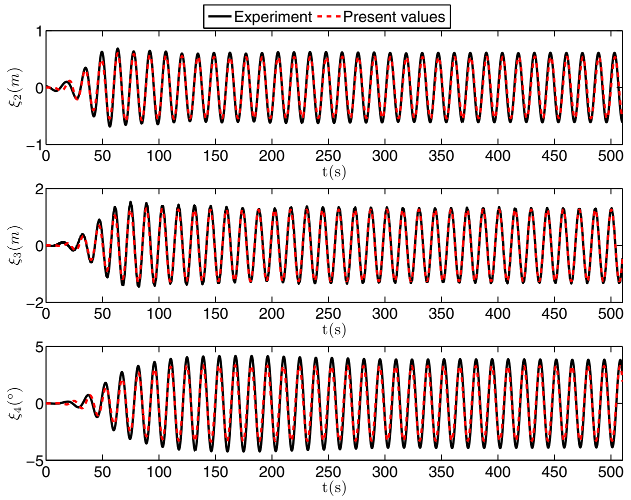

Fig. 39 Comparison between numerical and experimental motion time series for sway (ξ_2), heave (ξ_3) and roll (ξ_4), considering $C_{44} = 0.06C_{\mathrm{crit}}$

experiment considering transient and regular waves presented different amplitude values, which makes a perfect tuning of the damping coefficient impossible for both cases with the linear approach herein applied. In fact, for being a D.O.F. more susceptible to nonlinear effects, its results, especially on the resonant frequency range, are highly dependent on the incoming experimental wave amplitude, which justifies the differences observed also in the experimental results obtained by the two techniques applied in the experimental test (regular and transient waves). In spite of this fact, good predictions were obtained with the numerical method, pointing out the code capability to predict the motions of a floating body with more complex geometries than hemispheres and cylinders bodies.

6 Conclusion

The development of an in-house numerical code that deals with wave–body formulations which describe the interaction between floating bodies and free surface gravity waves under the assumption of potential flow theory was presented. This development is a first stage of a research that aims at, in a medium-term goal, considering nonlinear wave effects and the coupling of the present code to the TPN dynamic simulator of offshore systems, which also takes into account the effects of wind, current, risers and mooring lines.

The problem was addressed in a linear version, which enabled us to split up the total velocity potential in a sum of a disturbed wave potential and an analytic solution of an incoming wave field. This allowed us to change the problem variable to the disturbed wave potential only, avoiding the necessity of including a numerical wave maker to account for the incoming sea waves. Moreover, as the disturbed waves are generated from the body toward the free surface edge, we did not need to concentrate on a great number of free surface panels along all the domain, but to a very confined region near the body.

The inclusion of a second initial boundary value problem over the first one defined for the disturbed wave velocity potential was also discussed. Time domain simulations require a coupled treatment of the equations of the fluid motion and the body dynamics to guarantee an equilibrium of forces between the fluid and floating body at all times. Therefore, an accurate scheme for the calculation of time derivative of the velocity potential and consequently the pressure determination is essential for a consistent formulation. For the present calculations, we applied the linear acceleration potential which also satisfies Laplace's equation.

The numerical code was first tested by the calculation of the hydrodynamic loads in hemisphere and cylinder bodies, resulting from the well-known problems of diffraction and radiation. In addition, free floating simulations were also conducted to verify whether the procedures adopted to couple the fluid and body equations were correctly implemented or not. Convergence of the results with the increasing of the number of panels was also verified by performing several simulations with meshes of different resolutions. As expected, the higher the number of panels, the lower were the relative errors between the present calculations and the adopted reference values from WAMIT and [24]. As could be observed, these comparisons presented very good agreements, demonstrating that the numerical code developed so far was capable of predicting the hydrodynamic loads and motions caused by the wave–body interaction problem.

Free floating simulations with an FPSO hull were also conducted and the RAO of motions were verified through comparisons with experimental data obtained from tests carried out at the CH-TPN. The RAOS were obtained by applying an FFT analysis on the regular regime of the motion time series. Despite some small deviations specially concerning resonance peak values, the present results presented a good agreement with experimental data. Moreover, a direct comparison of numerical and experimental time series was also presented, in which not only the amplitudes but also the phases between the model motions could be verified. The results demonstrated that the numerical code developed was correctly implemented and capable of predicting the motions of a real offshore floating structure under the action of incoming regular waves.

Further development of the code has been done toward the implementation of higher-order methods, in which both the geometry and the solutions are described in terms of non-uniform rational B-spline (NURBS) surfaces. With this approach, the inclusion of current effects and the solution of the second-order problem becomes more suitable for tackling, since the spatial derivatives of the velocity potential may be calculated straightforwardly.

Acknowledgments The authors gratefully acknowledge Petrobras for sponsoring this research project and also for making the experimental data available for the verification of our method. Furthermore, the first and second authors acknowledge FAPESP for their scholarships (Proceedings No. 2010/08778-2 and Proceedings No. 2012/06681-7).

References

1. Lee CH, Newman JN (2004) In: Chakrabarti S (ed) Computation of wave effects using panel method, numerical models in fluid-structure interaction. WIT Press, Southhampton
2. Cummins WE (1962) The impulsive response function and ship motions. Symposium on Ship Theory at the Institut für Schiffbau der Universität Hamburg, pp 25–27
3. Stoker JJ (1957) Water waves. Interscience Publishers, New York
4. Gadd GE (1975) A method of computing the flow and surface wave pattern around full forms. The Royal Institution of Naval Architects
5. Dawson CW (1977) A practical computer method for solving ship-wave-problems. In: Proceedings of the second international conference on numerical ship hydrodynamics
6. Kring DC (1994) Time domain ship motions by a three-dimensional rankine panel method, PhD Thesis, Massachusetts Institute of Technology
7. Huang Y (1997) Nonlinear ship motions by a rankine panel method, PhD Thesis, Massachusetts Institute of Technology
8. Kim T, Kim Y (2013) Numerical analysis on floating-body motion responses in arbitrary bathymetry. Ocean Eng
9. Hess JL, Smith AMO (1967) Calculation of potential flow about arbitrary bodies. Prog Aerosp Sci 8:1–138
10. van Daalen EFG (1993) Numerical and theoretical studies of water waves and floating bodies, PhD thesis, Univeristy of Twente, The Netherlands
11. Tanizawa K (1995) A nonlinear simulation method of 3D body motions in waves: formulation of the method with acceleration potential (1st report). J Soc Naval Architect Jpn

12. Tanizawa K (2000) The state of the art on numerical wave tank. In: Proceedings of 4th Osaka colloquium on seakeeping performance of ships, pp 95–114
13. Danmeier DG (1999) A higher-order panel method for large-amplitude simulations of bodies in waves, PhD thesis, Massachusetts Institute of Technology
14. Koo W (2003) Fully nonlinear wave-body interactions by a 2D potential numerical wave tank, PhD thesis, Texas A and M University
15. Newman JN (1985a) Algorithms for free-surface green function. J Eng Mathematics 19:57–67
16. Newman JN (1985) The evaluation of free-surface green function. In: Proceedings of the 4th numerical ship hydrodynamics conference
17. Yang C, Noblesse F, Lhner R (2004) Comparison of classical and simple free-surface green functions. In: Proceedings of the fourteenth international offshore and polar engineering conference
18. Israeli M, Orzag SA (1981) Approximation of radiation boundary conditions. J Comput Phys 41:115–135
19. Prins H (1985) Time-domain calculations of drift forces and moments, PhD Thesis, Tecnische Universiteit Delft
20. Bunnik THJ (1999) Seakeeping calculations for ships, taking into account the non-linear stady waves, PhD Thesis, Tecnische Universiteit Delft
21. Boo SY (2002) Linear and nonlinear irregular waves and forces in a numerical wave tank. Ocean Eng 29:475–493
22. Shao YL (2010) Numerical potential-flow studies on weakly-nonlinear wave-body interactions with/without small forward speeds, PhD thesis, Norwegian University of Science and Technology
23. Zhen L, Bin T, De-zhi N, Ying G (2010) Wave-current interactions with threedimensional floating bodies. J Hydrodyn 22:229–240
24. Hulme A (1982) The wave forces acting on a floating hemisphere undergoing forced periodic oscillations. J Fluid Mech 121:443–463
25. Watai RA (2015) A time domain boundary elements method for the seakeeping analysis of offshore systems, PhD Thesis, University of Sao Paulo
26. Mello PC, Carneiro ML, Tannuri EA, Nishimoto K (2010) USP active absorption wave basin: from conception to commissioning. In: Proceedings of the ASME 2010 29th international conference on ocean, offshore and artic engineering, OMAE2010, Shangai